



HAL
open science

Combustion and Flame. Determination of spatially averaged consumption speed from spherical expanding flame: A new experimental methodology

M-E. Clavel, A. Vandael, Vincent Modica, Z. Chen, E. Varea, V. Moureau, B. Renou

► **To cite this version:**

M-E. Clavel, A. Vandael, Vincent Modica, Z. Chen, E. Varea, et al.. Combustion and Flame. Determination of spatially averaged consumption speed from spherical expanding flame: A new experimental methodology. Combustion and Flame, 2022, 235, pp.111720. 10.1016/j.combustflame.2021.111720 . hal-03706136

HAL Id: hal-03706136

<https://normandie-univ.hal.science/hal-03706136>

Submitted on 26 Nov 2023

HAL is a multi-disciplinary open access archive for the deposit and dissemination of scientific research documents, whether they are published or not. The documents may come from teaching and research institutions in France or abroad, or from public or private research centers.

L'archive ouverte pluridisciplinaire **HAL**, est destinée au dépôt et à la diffusion de documents scientifiques de niveau recherche, publiés ou non, émanant des établissements d'enseignement et de recherche français ou étrangers, des laboratoires publics ou privés.

Combustion and Flame

Determination of spatially averaged consumption speed from spherical expanding flame: a new experimental methodology.

--Manuscript Draft--

Manuscript Number:	CNF-D-21-00389R3
Article Type:	Full Length Article
Keywords:	Laminar burning velocity; spherically expanding flames; Stretch effects; consumption speed; Displacement speed
Corresponding Author:	Bruno Renou, Ph.D. UMR 6614 CORIA Saint-Etienne du Rouvray Cedex, FRANCE
First Author:	Marie-Eve Clavel
Order of Authors:	Marie-Eve Clavel Alexis Vandael Vincent Modica, PhD Zheng Chen, PhD Emilien Varea, PhD Vincent Moureau, PhD Bruno Renou, PhD
Abstract:	<p>Facilities using spherically expanding flame in closed vessels are generally used to report laminar burning velocities from extrapolated stretched flame speed. Considering the 1D planar reference case, flame displacement speed and consumption speed are rigorously identical. This is not true considering spherically expanding flames. While the flame displacement speeds are defined from a kinematic point of view, the consumption speed is linked to the integral of the reaction rate across the flame front. The latter is defined from a kinetic reference frame. Even though spherically expanding flames have been studied for decades, it is still challenging to experimentally determine the consumption speed. Recent developments define analytical expressions for the consumption speed and suggest experimental determination. One of the major issues consists in measuring the temporal evolution of the fresh gas density while the flame expands. In this work, an optical PIV-based method is developed to directly determine the fresh gas density ahead of the flame front and then the spatially averaged consumption speed. For the first time, experimental measurements of flame displacement speeds relative to fresh gases and burned gases, and spatially averaged flame consumption speeds are then reported for methane/air flames at different equivalent ratios. Experimental measurements are systematically compared with DNS which simulates the experimental geometry. A very good agreement is observed between experimental and numerical data irrespective to the equivalence ratio, underlying the robustness of the experimental methodologies. Finally, the sensitivity of the different flame speeds to flow confinement and extrapolation models is discussed.</p>

1
2
3
4
5
6
7
8
9
10
11
12
13
14
15
16
17
18
19
20
21
22
23

Determination of spatially averaged consumption speed from spherical expanding flame: a new experimental methodology.

14 M-E. Clavel^{a,c}, A. Vandael^a, V. Modica^a, Z. Chen^b, E. Varea^a, V. Moureau^a, B.
15 Renou^{a,*}

17 ^a*Normandie Univ., UNIROUEN, INSA Rouen, CNRS, CORIA, 76000 Rouen, France*

18 ^b*SKLTCS, CAPT, BIC-ESAT, College of Engineering, Peking University, Beijing 100871,*
19 *China*

20 ^c*Safran Aircraft Engines Villaroche, 77550 Moissy-Cramayel, France*

Abstract

24
25
26
27
28
29
30
31
32
33
34
35
36
37
38
39
40
41
42
43
44
45
46
47
48
49
50
51
52
53
54

Facilities using spherically expanding flame in closed vessels are generally used to report laminar burning velocities from extrapolated stretched flame speed. Considering the 1D planar reference case, flame displacement speed and consumption speed are rigorously identical. This is not true considering spherically expanding flames. While the flame displacement speeds are defined from a kinematic point of view, the consumption speed is linked to the integral of the reaction rate across the flame front. The latter is defined from a kinetic reference frame. Even though spherically expanding flames have been studied for decades, it is still challenging to experimentally determine the consumption speed. Recent developments define analytical expressions for the consumption speed and suggest experimental determination. One of the major issues consists in measuring the temporal evolution of the fresh gas density while the flame expands. In this work, an optical PIV-based method is developed to directly determine the fresh gas density ahead of the flame front and then the spatially averaged consumption speed. For the first time, experimental measurements of flame displacement speeds relative to fresh gases and burned gases, and spatially averaged flame consumption speeds are then reported for

55 *Corresponding author:

56 *Email address: renou@coria.fr (B. Renou)*

methane/air flames at different equivalent ratios. Experimental measurements are systematically compared with DNS which simulates the experimental geometry. A very good agreement is observed between experimental and numerical data irrespective to the equivalence ratio, underlying the robustness of the experimental methodologies. Finally, the sensitivity of the different flame speeds to flow confinement and extrapolation models is discussed.

Key words: Laminar burning velocity, Spherically expanding flames, Stretch effects, Consumption speed, Displacement speed

1. Introduction

The development of new kinetic schemes requires efficient validation on ignition delays time, major and/or minor species profiles and unstretched laminar burning velocity S_L^0 data. For 1D unstretched planar premixed flame, S_L^0 represents the rate at which the fresh gases are consumed through the flame front. By integrating the transport equation of the fuel mass fraction through the flame domain, one can derive the expression of the laminar burning velocity for 1D planar flames [1],

$$S_L^0 = \frac{1}{\rho_u (Y_{F,b} - Y_{F,u})} \int_{-\infty}^{+\infty} \dot{\omega}_F dx \quad (1)$$

where ρ_u is the fresh gas density, $\dot{\omega}_F$ is the fuel reaction rate and $Y_{F,b}$ and $Y_{F,u}$ are the fuel mass fractions in burned and fresh gases, respectively. The upper script 0 refers to the 1D and unstretched conditions. From Eq. (1), the laminar burning velocity S_L^0 is equivalent to a *consumption speed* and corresponds to the fuel mass rate which enters the flame front. This expression of the laminar burning velocity is valid for any major species k . For the 1D planar configuration, the laminar burning velocity can also be defined as a *kinematic quantity* which is called the *density weighted flame displacement speed* [2],

$$\widetilde{S}_d^0 = \frac{\rho}{\rho_u} (\mathbf{S}_f - \mathbf{u}) \cdot \mathbf{n} = S_L^0 \quad (2)$$

1
2
3
4
5
6
7
8
9 The density-weighted displacement speed is defined to a specified
10 temperature iso-surface. The temperature gradient defines the unit normal \mathbf{n}
11 to the flame surface, with \mathbf{n} pointing towards the fresh reactants. $S_f = \mathbf{S}_f \cdot \mathbf{n}$
12 is the absolute flame speed or propagation speed, and $u = \mathbf{u} \cdot \mathbf{n}$ is the local
13
14 20 is the absolute flame speed or propagation speed, and $u = \mathbf{u} \cdot \mathbf{n}$ is the local
15 flow velocity normal to the temperature iso-surface. ρ is the local flow density
16 obtained at the flame iso-surface where u is defined.
17

18
19 Laminar burning velocity is one of the few fuel parameters which can
20 be experimentally measured at relevant conditions for engines or combustion
21 chamber applications [3]. Among the different techniques, experimental facility
22 25 chamber applications [3]. Among the different techniques, experimental facility
23 using spherically expanding flame is generally chosen as it offers flexibility in
24 terms of initial conditions.
25

26
27 Several methods have been developed to measure flame speeds from
28 expanding flames in confined vessels. They should be considered as
29
30 30 complementary.

31
32 The constant volume method is quite old and makes it possible to obtain
33 flame speed values for high pressure and temperature conditions from the
34 time analysis of the pressure signal in the combustion chamber and from
35 a thermodynamic model for the mass fraction of burnt gases. Recently,
36
37 35 experimental and numerical works have provided original solutions to overcome
38 these models and demonstrated the potential of this method [4–6].
39

40
41 The constant pressure method is widely used for a broad range of operating
42 conditions (including low pressure) and fuel compositions. For this approach,
43 spherical expanding flames are stretched due to the interaction between flame
44
45 40 propagation and flow, and S_L^0 is reported using extrapolation procedures to zero
46 stretch. Discussions about linear and non-linear models can be found in [7] for
47 instance, and effects of finite flame thickness in extrapolation models in [8, 9].
48
49

50
51 In the following, all the developments concern the constant pressure method.
52 In constant pressure method, unstretched laminar burning velocity is commonly
53
54
55
56
57
58
59
60
61
62
63
64
65

1
2
3
4
5
6
7
8
9
45 reported from density-weighted displacement speed relative to the burned gases,

$$\widetilde{S}_{d,b} = \frac{\rho_b}{\rho_u} (\mathbf{S}_f - \mathbf{u}_b) \cdot \mathbf{n} \quad (3)$$

10
11
12
13
14 This equation is systematically simplified into,

$$\widetilde{S}_{d,b} \simeq \frac{\rho_b^{eq}}{\rho_u} \frac{dR}{dt} \quad (4)$$

15
16
17
18
19
20 where ρ_b^{eq} is the burned gas density at adiabatic thermodynamic and
21 chemical equilibrium conditions. dR/dt is the absolute flame speed, S_f , deduced
22 from the time derivative of the flame radius, R . R is experimentally obtained
23 from high-speed schlieren, shadowgraphy or tomographic recordings. Note that
24
25 50 from high-speed schlieren, shadowgraphy or tomographic recordings. Note that
26 the burned gases are assumed to be at rest ($u_b = 0$). So, in these conditions,
27 Eq. (4) becomes the easiest way to experimentally determine the laminar
28 burning velocity. However, the hypothesis required to reach this formulation are
29 sometimes not fully verified, involving many biases on the S_L^0 determination.
30
31
32
33 55 Indeed, for small combustion chamber [10], for low pressure [11] and when
34 radiation is non-negligible [12], these approximations fail and other experimental
35 approaches are necessary.
36

37
38 Recent developments in PIV post-processing [13–15] allow to directly
39 measure the local fresh gas velocity, u_u , ahead of the flame front. This region is
40
41 60 characterized by high local velocity gradient, which makes the measurements
42 very difficult to perform. New algorithms were developed and the density
43 weighted displacement speed relative to the fresh gases, $\widetilde{S}_{d,u}$, can be now
44 experimentally determined,
45
46

$$\widetilde{S}_{d,u} = \left(\frac{dR}{dt} - u_u \right) \quad (5)$$

47
48
49
50
51 The fresh gas velocity u_u is approximated experimentally by the maximum of
52
53 65 fresh gas velocity which occurs at the entrance of the preheat zone. $\widetilde{S}_{d,u}$ allows
54 a direct measurement of laminar flame speed, without assumptions on the state
55 of the burned gases, and on the velocity field. This approach must be considered
56
57
58

1
2
3
4
5
6
7
8
9 to report laminar flame speed when conditions required to use Eq. 4 fail.
10 Consequently, the two kinematic approaches (Eqs. 3 and 5) are complementary
11
12 and must be used together to address the difficult task to measure laminar
13
14 burning velocity with the constant-pressure method.

15 The two previous flame speed definitions are related to kinematic
16 information. It is however possible to introduce the *consumption speed* based
17 on the integral of the reaction rate. Similar to 1D condition (Eq. 1), a local
18
19 consumption speed can be introduced and calculated in spherical expanding
20
21 flames [16]. This definition is appropriate for unidirectional flows, e.g., planar
22
23 or spherical flames, where the normal to the flame is properly defined, but it
24
25 can not be measured experimentally. To overcome this difficulty, *the spatially*
26
27 *averaged consumption* speed was introduced a long time ago by normalizing
28
29 the global consumption rate, obtained by integrating the fuel reaction rate
30 throughout the entire combustion volume by the flame surface area. Fiock and
31 Marvin [17], Bradley and Mitcheson [18] or more recently Bonhomme et al. [19]
32 developed theoretical approaches for the spatially averaged consumption speed
33 of the deficient species. Lefebvre et al. [20] recently developed a generalized
34
35 expression for any major species k . However, the authors concluded that only
36
37 the equation of deficient species can be experimentally used since it does not
38
39 require the determination of ambiguous burned gas parameters such as ρ_b or
40
41 the mass fraction of species k in the burned gases. These parameters are not
42
43 necessarily spatially homogeneous and are almost difficult to measure. The
44
45 expression of the spatially averaged consumption speed for the deficient species
46
47 k is [20],

$$\begin{aligned}
 \langle S_c \rangle &= \langle S_{c,k} \rangle = S_f - \frac{(R_0^3 - R_{f,k}^3)}{3R_{f,k}^2} \frac{1}{\rho_u} \frac{d\rho_u}{dt} \\
 &= -\frac{1}{\rho_u Y_{k,u} R_{f,k}^2} \int_0^{R_0} \dot{\omega}_k r^2 dr
 \end{aligned} \tag{6}$$

48
49
50
51
52
53
54
55 where $R_{f,k}$ is an equivalent flame radius based on the integral of a progress
56
57
58

variable based on the partial density of species k and the radius. $R_{f,k}$ is given by

$$R_{f,k} = \sqrt[3]{\int_0^{R_0} \left(1 - \frac{\rho Y_k}{\rho_u Y_{k,u}}\right) 3r^2 dr} \quad (7)$$

In this equation, R_0 is the combustion chamber radius. Consequently, the spatially averaged consumption speed $\langle S_c \rangle$ corresponds to the global consumption rate normalized by the surface defined by the radius $R_{f,k}$ based on the total mass of species k contained into the sphere of radius $R_{f,k}$. For lean and stoichiometric mixtures, $k = \text{Fuel}$, and for rich conditions, $k = O_2$. It was recently shown that the isotherm corresponding to the flame radius $R_{f,k}$ is very closed to that of experimental radius obtained by laser tomography [20]. This spatially averaged consumption speed is therefore not exactly equal to the local consumption speed (Eq.1) [16], but it represents a convenient way to experimentally report the global fuel consumption rate, from scalar measurements. A promising method to measure the spatially averaged consumption speed in a closed vessel was presented in the numerical work of Bonhomme et al. [19]. The authors proposed to combine both the temporal evolution of the flame radius $R_f(t)$ and the internal chamber pressure $P(t)$ assuming an isentropic compression for the fresh gases, as

$$\frac{1}{\rho_u} \frac{d\rho_u}{dt} = \frac{1}{\gamma_u P} \frac{dP}{dt} \quad (8)$$

The *spatially averaged consumption speed* yields

$$\langle S_c \rangle = \frac{dR_f}{dt} - \frac{(R_0^3 - R_f^3)}{3R_f^2} \frac{1}{\gamma_u P} \frac{dP}{dt} \quad (9)$$

Prima facie, Eq. 9 seems to be a good candidate for the evaluation of the consumption speed as it only requires the temporal evolution of the flame radius and the pressure signal $P(t)$. However, from an experimental point of view, the values of the consumption speed could lack accuracy since this formula is based on the difference of two large numbers. This was originally

1
2
3
4
5
6
7
8
9 mentioned by Andrews and Bradley [21]. Therefore, the experimental accuracy
10 of the pressure measurement must be excellent to avoid any noise during the
11 time derivative computation of the pressure signal. It implies that the pressure
12 sensor has to be accurate enough during the early stages of flame development
13
14
15 (pre-pressure period), where the pressure rise is very small (in the range of
120 hundreds Pascal) and at the same time, the pressure sensor must also be
16 capable of withstanding high pressure loads due to the combustion process in
17 a constant volume chamber. From these observations, the consumption speed
18 can therefore be estimated from Eq. (6) where the fresh gas density needs to
19
20
21
22
23 be evaluated, or from Eq. (9) where the pressure trace needs to be accurately
125 recorded.
24
25
26
27

28 The aim of this study is therefore three-fold:
29

- 30 • First, a new experimental approach to estimate the instantaneous density
31 field ahead of the flame front is developed and used to report the
130 spatially averaged consumption speed for spherical expanding flames.
32 It is based from the mass conservation written for a material control
33 volume, and requires the measurement of the local fresh gas velocity.
34 This methodology is validated by comparing DNS simulations of laminar
35 spherically expanding flame and experimental data for methane/air
36
37
38
39
135
40
41
42
43
44
45
46
47
48
140
49
50
51
52
53
54
55
56
57
58
59
60
61
62
63
64
65
- The experimental methodology initially developed by [14] to report fresh
gas velocity profile ahead of the flame front is reconsidered and improved,
to provide more accurate data. An extensive work of optimization of
post-processing routines, camera properties and laser frequencies are
conducted on classical methane/air mixtures at atmospheric conditions.
A direct comparison with DNS data is also performed to assess the quality
of the post-processing steps.
- Finally, the suitability of the spatially averaged consumption speed
formulation ($\langle S_c \rangle$) and kinematic approaches ($\widetilde{S}_{d,u}$ and $\widetilde{S}_{d,b}$) for lean, rich

1
2
3
4
5
6
7
8
9 and stoichiometric methane/air flames is discussed from both experimental
10 and numerical data.
11

12 13 14 **2. Experimental and numerical apparatus**

15
16 In this section, the experimental setup for flame speed measurements is
17 briefly described. Details on the numerical simulations performed with the DNS
180 code (A-SURF) are also presented.
19
20

21 *2.1. Experimental setup*

22
23 The apparatus and post-processing methods are described in detail in [14, 22]
24 and are briefly reminded. Experiments are conducted in a spherical stainless
25 steel combustion chamber with an equivalent chamber radius $R_0 = 8.243$ cm.
26
155 The mixture is seeded with micronical silicon oil droplets with a theoretical
27 boiling temperature of $T = 580K$. High-speed laser tomography technique is
28 used to capture the temporal evolution of the flame front and particle images
29 by using a circle least-square fitting method. A double cavity Nd:YLF laser
30 (Darwin Dual, Quantronix), delivering 6 mJ pulses at 527 nm and at 5 kHz,
31 is used to illuminate seeding particles. A high-speed camera (Photron Fastcam
32 SA1.1) records 12-bit images of 1024 x 1024 pixels² at the same frequency of
33 5 kHz. The camera is perpendicular to the laser sheet. The magnification
34 ratio is set to 0.04746 mm/px. In addition to the measurements from optical
35 diagnostics, the pressure trace is recorded during the flame propagation using
36 a dynamic pressure transducer *Kistler 7001*, directly placed into the vessel in
37 order to avoid disturbance or attenuation. This sensor, which has a natural
38 frequency of 70 kHz, has been selected since it fits as best as possible the
39 existing setup while keeping the best dynamics. Moreover, the sensor is resistant
40 enough to high pressure loads. For each experimental condition, experiments
41 are performed 10 times and all values of stretched flame speeds are based on
42 these series of 10 measurements. Methane/air mixtures are investigated for very
43 lean ($\phi = 0.7$), stoichiometric and rich ($\phi = 1.2$) conditions, with a pressure of 1
44 atm and a temperature of 293K.
45
46
47
48
49
50
170
51
52
53
54
55
56
57
58

1
2
3
4
5
6
7
8
9 175 *2.2. Numerical simulation with A-SURF code*

10 Spherical flame propagation is simulated using the DNS code A-SURF.
11 The simulation domain reproduces the experimental apparatus described above
12 in terms of chamber geometry and thermodynamical properties. A-SURF
13 solves the one-dimensional, unsteady, compressible, conservation equations for
14 a multi-component reactive flow in spherical coordinates using the finite volume
15 method. The details on governing equations, numerical schemes, and code
16 validation can be found in [23]. Simulations are performed for CH_4/air flames
17 with the *GRI-mech 3.0* kinetic scheme [24]. It is noted there are several recent
18 kinetic models for methane oxidation. According to Wang et al. [25], there is
19 good agreement among laminar flame speeds predicted by different mechanisms
20 for ambient conditions and large discrepancy appears only for engine-relevant
21 conditions with pressure above 20 atm. Since here we consider the ambient
22 conditions for which GRI-mech 3.0 was optimized, GRI-mech 3.0 is used in
23 our simulations. Initial conditions are atmospheric thermodynamic conditions,
24 *i.e.* a temperature of 293 K and a pressure of 1 atm. In all the simulations,
25 the mixture is initially static. In order to maintain adequate resolution of the
26 propagating flame, dynamically adaptive mesh is utilized in A-SURF with a
27 finest grid size of 8 μm . It is noted that radiation heat loss is not considered
28 here. Since the equivalence ratios are not close to the flammability limits of
29 methane/air mixtures and the corresponding laminar flame speeds are above 15
30 cm/s, radiation heat loss has negligible effect on propagating spherical flames
31 whose radii are below 2 cm [26]. This DNS database will be used for a direct
32 and blind comparison with the different laminar flame speeds reported from the
33 experiments, and the validation of the post-processing routines as well.

34
35
36
37
38
39
40
41
42
43
44
45
46
47
48
49 200 Unstretched laminar burning velocities are computed by Cantera [27] from
50 the one-dimensional freely-propagating configuration, by using the same kinetic
51 scheme [24] and the same operating conditions ($T = 293 K$, $P = 1 atm$).
52 In these simulations, the mixture-averaged diffusion model is considered. The
53 computational domain is from 0 to 5.0 cm. The minimum values of the gradient
54 and curvature for the last iteration are set to 0.02.
55
56
57
58
59
60
61
62
63
64
65

3. Measurements of fresh gas velocity profiles ahead of the flame front

3.1. Principles

An in-house PIV post-processing technique is used to compute the fresh gas velocity field ahead of the flame front, to report $\langle S_c \rangle$ and $\widetilde{S_{d,u}}$. For two successive tomographic images where the flame radius R_T can be extracted, the algorithm defines a region of interest (ROI) around the spherical flame. The ROI is an angular sector of the fresh gases with an angle θ which is adjusted to 320° which fits the flame contour of a radius R_T . The width of the ROI is restricted to 110 pixels (5.22 mm), where the velocity profiles are measured (Figure 1). This ROI is then dewarped into a Cartesian coordinate system using a bilinear interpolation scheme. An interrogation window (IW) with a width varying from 1 to 5 pixels is located within this ROI. A matching method based on a two-dimensional normalized cross-correlation is used between IWs of the two successive ROIs. First, the best correlation between both IWs is obtained by shifting only the first IW in increments of one pixel in the direction normal to the flame front. The location of the maximum of correlation (Δr_1^{opti}) obtained from a sub-pixel fit (7 points Gaussian) gives the fresh gas velocity u ahead of the flame front at the location of the first IW, so that

$$u(t^*, \Delta r_2) = \frac{R_T(t^* + \Delta t) - R_T(t^*)}{\Delta t} + \frac{\Delta r_2 - \Delta r_1^{opti}(t^*)}{\Delta t} \quad (10)$$

where $R(t^*)$ and $R(t^* + \Delta t)$ are the flame radii at time t^* and $t^* + \Delta t$, Δt is the time between two successive images and Δr_1^{opti} is the optimum displacement of the first IW obtained for the displacement of the second IW, Δr_2 . Fixing the second IW and searching the best correlation on the first one avoids problems of evaporated droplets. To characterize the velocity profile ahead of the flame, the second stage of post-processing consists in moving the second IW by step of one pixel (Δr_2) in the direction normal to the flame front. For each position of this window, the first step of the template matching procedure is restarted. Original details of the procedure can be found in [14]. There is a compromise to find on the thick of the interrogation window (IW) in the ROI. The thicker

1
2
3
4
5
6
7
8
9
10
11
12
13
14
15
16
17
18
19
20
21
22
23
24
25
26
27
28
29
30
31
32
33
34
35
36
37
38
39
40
41
42
43
44
45
46
47
48
49
50
51
52
53
54
55
56
57
58
59
60
61
62
63
64
65

the IW, the better the correlation since much more droplets will be included
 235 in the correlation. But the spatial filtering of the velocity profiles will be more
 important and the maximum of the velocity profile would not be captured. We
 did several tests, and the conclusions give that the compromise is at 2 pixels.
 It is worth noting that the first term in the right hand side of Eq. 10 is equal
 to the flame propagation speed $S_f \cdot \mathbf{n}$ approximated by finite difference.

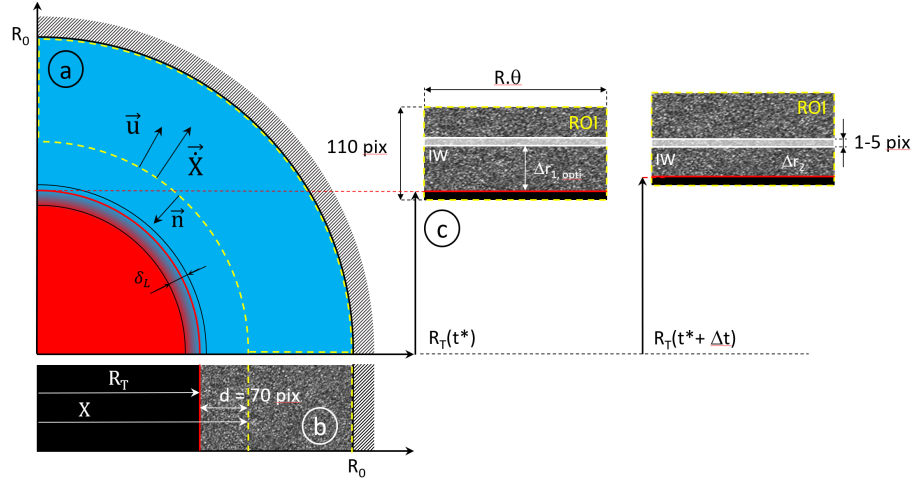


Figure (1) Sketch of flame kernel propagation in the confined combustion chamber of radius R_0 . (a) A quarter of the flame with a flame thickness δ_L is represented. The red curve is associated to the flame contour obtained by laser tomography and corresponds to the oil droplet evaporation isotherm. (b) A 1D view of a dewarped tomographic image with the corresponding tomographic flame radius R_T . The control volume used for the determination of fresh gas density is represented with yellow dotted lines. (c) Similar dewarped tomographic images at two successive times used for the determination of the fresh gas velocity profiles ahead of the flame front. The ROI is represented by a yellow dotted line rectangle and the IW is the gray zone with an adjustable width of 1-5 pixels.

240 *3.2. Improvement and validation of the experimental methodology*

The availability of the DNS database is a good opportunity to revisit
 and optimize the post-processing routines which were originally developed in
 [14]. First, we address the question of the tomographic image post-processing,
 since the image quality impacts strongly the contour detection and correlation
 245 processes. An automatic contrast adjustment procedure of tomographic images
 is performed by using a linear stretching of intensity range. At the same time,
 laser sheet in-homogeneity is corrected by using temporally averaged seeded

tomographic recordings (without flames). Consequently, black and white are saturated to make flame front detection easier and particles more identifiable.

In a second step, the interval time between two-successive images must be considered since it may impact the accuracy of the distance Δr between the value of the optimum displacement of the first IW $\Delta r_1^{opti}(t^*)$ with the value of the displacement of the second IW Δr_2 (Second term of the RHS in Eq. 10). The classical problem of correlation peak fitting procedure is clearly evidenced in Figure 2, where different correlograms have been obtained for different values of Δt . The laser frequency is kept constant at $f = 5000Hz$, and the images are processed with a $\Delta t = n/f$, n varying from 1 to 4. For each, a basic 7-points Gaussian fit is used to report the values of $\Delta r_1^{opti}(t^*)$. The lower the interval time Δt , the smaller the values $\Delta r_1^{opti}(t^*)$, and the greater the impact of the accuracy of the sub-pixel position of the maximum correlation peak on $\Delta r_1^{opti}(t^*)$. However, a high interval time may act as a low-pass spatial filtering when computing the fresh gas velocity which may fail to capture the maximum flow velocity. From our operating conditions, the best compromise seems to get a minimum value of Δr around 3 pixels which ensure a acceptable uncertainty and a spatial resolution of the velocity profile. Consequently, image frequency (nominal frequency or a fraction of the nominal frequency) is selected according to the flame propagation speed values for a specific operating conditions.

From the last improvements which have been discussed previously, some numerical and experimental profiles of the fresh gas velocity are reported in Figure 3 for two different equivalence ratios and two different flame radii. These selected plots are representative of the experimental measurements. At the same time, numerical temperature profiles are plotted. Due to inherent time shift from the numerical initialization of the flame kernel, computations and experimental data are time-scaled for a similar radius. The shift in time is as low as $200 \mu s$ which is more or less one experimental time step. The experimental velocity profiles obtained from the methodology presented above are plotted with black open circles. The fresh gas velocity at the entrance of the flame front, u_u , is obtained from the maximum (filled red diamond) of a

1
2
3
4
5
6
7
8
9
10
11
12
13
14
15
16
17
18
19
20
21
22
23
24
25
26
27
28
29
30
31
32
33
34
35
36
37
38
39
40
41
42
43
44
45
46
47
48
49
50
51
52
53
54
55
56
57
58
59
60
61
62
63
64
65

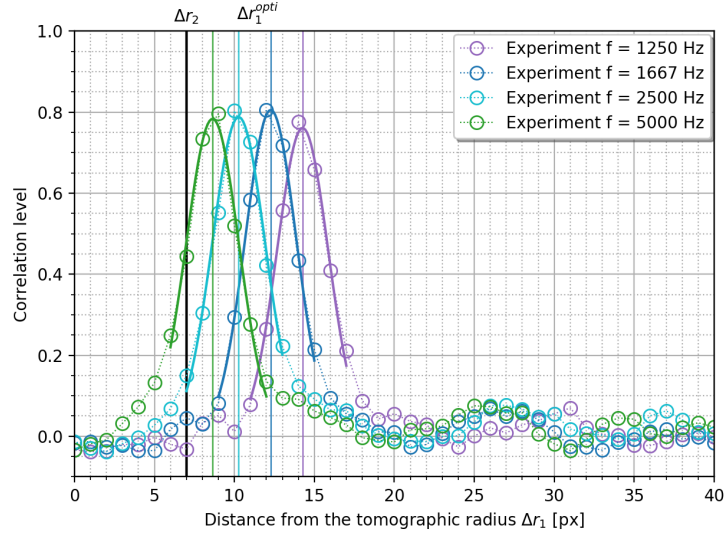


Figure (2) Correlation peaks (open circles) and corresponding 7-points Gaussian fit (continuous lines) for different interval times between two successive images. Value of Δr_2 is set to 7 pixels, corresponding to a location in the fresh gas velocity profiles close to the maximum values. Results for $\phi = 1$, and $t^* = 7.0 \text{ ms}$

6^{th} order polynomial fit from the first point to 1.3 mm (continuous red line).

280 The experimental velocity data, $u(r)$, in the decreasing zone (green zone) is fitted with the theoretical model suggested by Poinso et al. [1], following a $(R_0^3 - r^3)/r^2$ shape. Simultaneously, the experimental and numerical radii at the maximum fresh gas velocity are reported for a quantitative comparison between experiments and simulations. This figure highlights the capability of
285 the experimental methodology to report the gas velocity profiles both for the fresh gas side and in the preheat zone up to the evaporation of oil droplets accurately. The spatial resolution of the measurements is high enough to capture the maximum of the gas velocity which occurs at the entrance of the preheat zone. The interval times in two successive images have been adapted such as
290 the particle displacement at the maximum velocity profiles remains close to 3 pixels, as suggested above. One can notice also the perfect agreement of the experimental profiles with the numerical data.

Regarding Fig. 3, it is clear that the maximum of fresh gas velocity doesn't peak exactly at T_u but at a slightly higher temperature. Numerical data analysis

1
2
3
4
5
6
7
8
9 shows that this temperature is around 310 K and remains almost constant as
10 the flame propagates. This is very similar to the results presented in [28].
11 Consequently, the experimental displacement speed corresponds to
12

$$\widetilde{S}_{d,u}^{Exp} = \left(\frac{dR}{dt} - u_{g,max} \right) \quad (11)$$

13
14
15
16
17
18 where $u_{g,max}$ is the velocity at which the fresh gas velocity is maximum. We
19 assume implicitly equality between the definition of $\widetilde{S}_{d,u}$ from Eq. 5 and $\widetilde{S}_{d,u}^{Exp}$
20 from Eq. 11. This observation underlines also the difficulty to select the fresh
21 300 gases iso-surface when considering the displacement speed relative to the fresh
22 gases as it was originally discussed by Gianakopoulos et al. [2] and Jayachandran
23 et al. [28]. The choice of the fresh gas temperature as a reference location for
24 the determination of $S(d, u)$ is poorly conditioned and should be used with
25 care. However, even with this limitation, this approach must be considered as
26 305 a complementary to the classical methodology that might introduce issues due
27 to unknown fuel chemistry and burned gas composition, differential diffusion or
28 radiation effects, and low pressure as mentioned in the work of Varea et al. [29],
29 Jayachandran et al. [30] and Faghieh et al. [11]. It is worth noting that this
30 method is also limited by the flame thickness. The thinner the flame front, the
31 more difficult it becomes to capture and spatially resolve the maximum velocity.
32 Consequently, this approach is not suited for high pressure conditions but it is
33 rather well adapted for low pressure conditions (large flame thickness), when
34 the assumptions used to apply Eq. 4 fail.
35
36
37
38
39
40
41
42
43
44
45
46
47
48
49
50
51
52
53
54
55
56
57
58
59
60
61
62
63
64
65

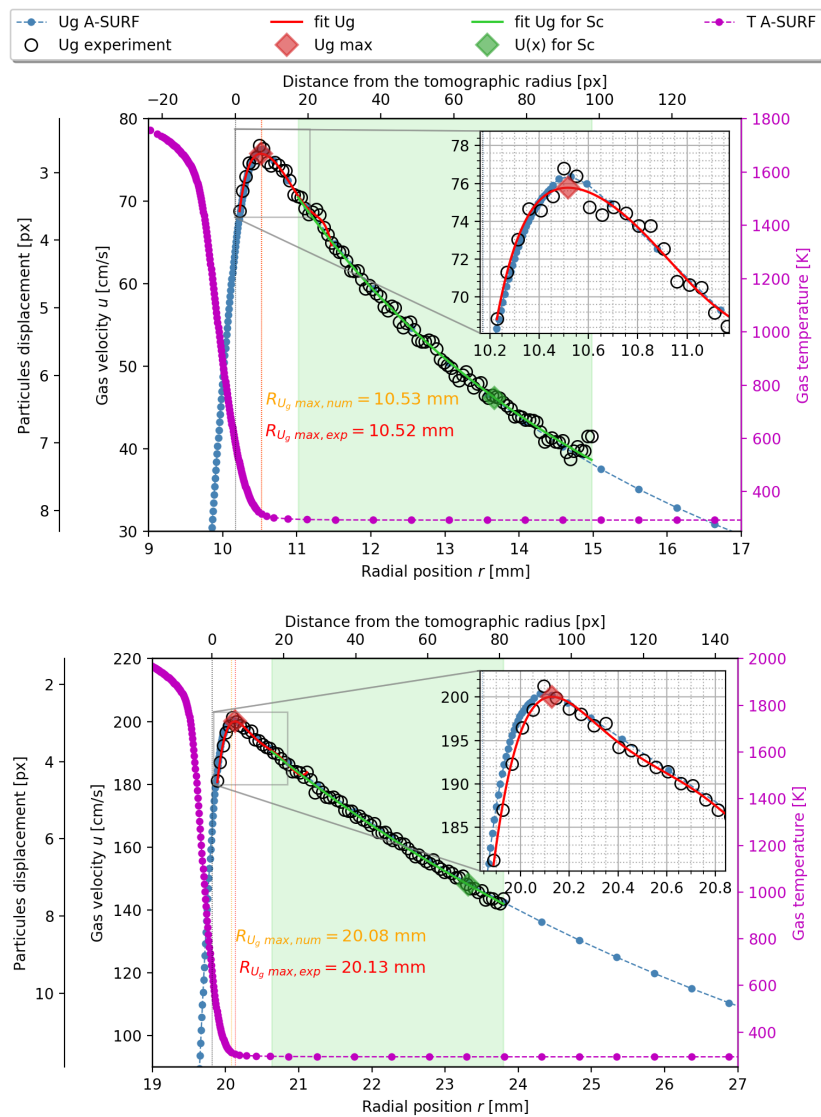


Figure (3) Fresh gas velocity and temperature profiles from experimental and numerical data, for two different operating conditions. (Top) Methane/air flame ($\phi = 0.7$ and $R_T = 15.2$ mm) and (Bottom) Methane/air flame ($\phi = 1.0$ and $R_T = 19.8$ mm)

1
2
3
4
5
6
7
8
9
10
11
12
13
14
15
16
17
18
19
20
21
22
23
24
25
26
27
28
29
30
31
32
33
34
35
36
37
38
39
40
41
42
43
44
45
46
47
48
49
50
51
52
53
54
55
56
57
58
59
60
61
62
63
64
65

315 **4. A new tool to determine the fresh gas density in freely propagating spherical expanding flames**

4.1. *Theoretical developments*

From its definition, the fresh gas density corresponds to the ratio between the mass of fresh gases and the volume it occupies. The temporal evolution of the fresh gas density can be estimated by determining the flux entering and/or leaving through the edges of a fixed volume. This flux is directly linked to the fresh gas velocity, a quantity which can be measured from PIV experiments. However, operating with a fixed volume is problematic since the flame propagates and might reach the edges of the fixed volume, therefore leading to unsuccessful PIV post-processing. Consequently, another type of analysis must be considered. In the present study, we propose to integrate the continuity equation in space considering an arbitrary volume $V_a(t)$ to allow an estimation of the fresh gas density temporal evolution, $\rho_u(t)$, while the flame expands. Let's consider a material control volume $V_m(t)$. The latter is defined such as it moves with the fluid so that the velocity at one point of its bordering surface is equal to the local fluid velocity U . The mass conservation equation without sources or sink terms is

$$\frac{d}{dt} \int_{V_m(t)} \rho dV = 0 \tag{12}$$

According to the transport theorem, an arbitrary control volume $V_a(t)$ which coincides with $V_m(t)$ at time t but doesn't necessarily move at the fluid velocity can be introduced and Eq. (12) is

$$\frac{d}{dt} \int_{V_m(t)} \rho dV = \frac{d}{dt} \int_{V_a(t)} \rho dV + \oint_{A_a(t)} \rho (\mathbf{u} - \dot{\mathbf{X}}) \cdot \mathbf{n} dA \tag{13}$$

where $\dot{\mathbf{X}}$ is the local velocity of the area $A_a(t)$ bordering the volume $V_a(t)$ and \mathbf{u} is the fluid velocity at the location X . Using an arbitrary volume is more convenient in experiments since the boundaries of the surface can be well selected. The sketch in Fig. 1 shows a spherical volume (only a quarter is

represented) which uniquely contains fresh gases from a radius $R = X$ to the vessel wall at $R = R_0$. Note that X is adjusted so that the distance d to the flame front is kept constant at each time step. Integrating Eq. (13) between time t^n and t^{n+1} yields

$$\frac{(\int \rho dV)^{n+1} - (\int \rho dV)^n}{t^{n+1} - t^n} - \oint_{A_a(t^{n+1/2})} \rho (u - \dot{X}) dA = 0 \quad (14)$$

Note that only the radial component is considered as the geometry is spherical. Assuming that the density at time step $n + 1/2$ is the average density between time $t = n$ and $t = n + 1$, one can estimate the temporal fresh gas density evolution at each time step as

$$\rho_u^{n+1} = \rho_u^n \frac{\left[\frac{R_0^3 - (X^n)^3}{3\Delta t} + \frac{1}{2} \left(X^{n+\frac{1}{2}} \right)^2 \left(u^{n+\frac{1}{2}} - \dot{X}^{n+\frac{1}{2}} \right) \right]}{\left[\frac{R_0^3 - (X^{n+1})^3}{3\Delta t} - \frac{1}{2} \left(X^{n+\frac{1}{2}} \right)^2 \left(u^{n+\frac{1}{2}} - \dot{X}^{n+\frac{1}{2}} \right) \right]} \quad (15)$$

with $X^{n+\frac{1}{2}} = \frac{X^{n+1} + X^n}{2}$ and $\dot{X}^{n+\frac{1}{2}} = \frac{X^{n+1} - X^n}{\Delta t}$. This equation requires the initial fresh gas density ρ_u^0 , the position X of the area $A_a(t)$ at each time step and the fresh gas velocity u through the area $A_a(t)$ between two consecutive time steps. This later is available unambiguously thanks to the developments presented above. The experimental method for determining these parameters as well as its validation are presented in the next section.

4.2. Validation from DNS data

Direct numerical simulations of CH_4/air flames at atmospheric pressure and temperature are used to access the time evolution of the fresh gas density. It is worth noting that the exact same methodologies, *i.e.* post processing techniques, are used for both experimental and numerical data. This induces consistency for comparisons. From the numerical simulations, the temporal fresh gas density evolution is evaluated using Eq. (15). This equation written in a discrete sense is computed with the position X which corresponds to the edge of a control volume and the velocity u of the fresh gases at this specific position X . Moreover,

1
 2
 3
 4
 5
 6
 7
 8
 9 from the simulations, the fresh gas density is also directly available. Therefore,
 10 one can evaluate the suitability of the Eq. (15) to report the fresh gas density,
 11 directly from the DNS. The results are shown in Figure 4 (Top). Note that the
 12 365 variables X and u have been computed from DNS data at an acquisition rate
 13 equal to the experimental one, *i.e.* 5 kHz . A perfect agreement between the
 14 fresh gas density from the simulations and the one calculated using Eq. (15) from
 15 the simulations are reported. This result confirms the reliability of Eq. (15) to
 16 accurately determine the fresh gas density ahead of the flame front. Moreover,
 17 370 an acquisition rate of 5 kHz seems to be sufficient enough to describe well the
 18 temporal evolution of the fresh gas density. In Eq. 15, the parameter X is
 19 defined according to the flame front position so that $X = R_T + d$, where d is
 20 a constant. The distance d should be set to avoid the influence of the preheat
 21 zone, so that the velocity profile displays a decreasing behavior, following a
 22 $1/R^2$ shape. This condition is satisfied when $d \geq 1 - 2\text{ mm}$. Effects of larger
 23 values d on the calculation of the compression term $1/\rho_u \cdot d\rho_u/dt$ are reported
 24 in Fig. 4 from the simulations. Relative differences of the rate of change of the
 25 fresh gas density calculated at $d = 1.2\text{ mm}$ and $d = 3.5\text{ mm}$ are marginal, and
 26 375 demonstrate very negligible effects of the distance d on the compression term.
 27 For the experimental determination of ρ_u , the distance d will be set to 70 pixels
 28 (3.3 mm). This value of $d = 70$ pixels is extracted from the velocity profile fit
 29 in Figure 3 and corresponds to the green fill diamond.
 30
 31
 32
 33
 34
 35
 36
 37
 38
 39
 40
 41
 42
 43
 44
 45
 46
 47
 48
 49
 50
 51
 52
 53
 54
 55
 56
 57
 58
 59
 60
 61
 62
 63
 64
 65

4.3. Application to experimental data and validation

385 Experimental data are processed to estimate the temporal evolution of the
 386 fresh gas density from Eq. (15). The main difficulty remains in the ability
 387 to accurately measure the parameter X , the position of the area $A_a(t)$ at
 388 each time step, and u , the fresh gas velocity through the area $A_a(t)$ between
 389 two consecutive time steps. Both experimental and numerical data of the
 390 compression term $1/\rho_u \cdot d\rho_u/dt$ plotted against the flame radius are reported in
 Fig. 5 for different equivalence ratio. Note that the experimental repeatability
 –shot-to-shot variation– is shown by plotting the 10 experimental trials. A

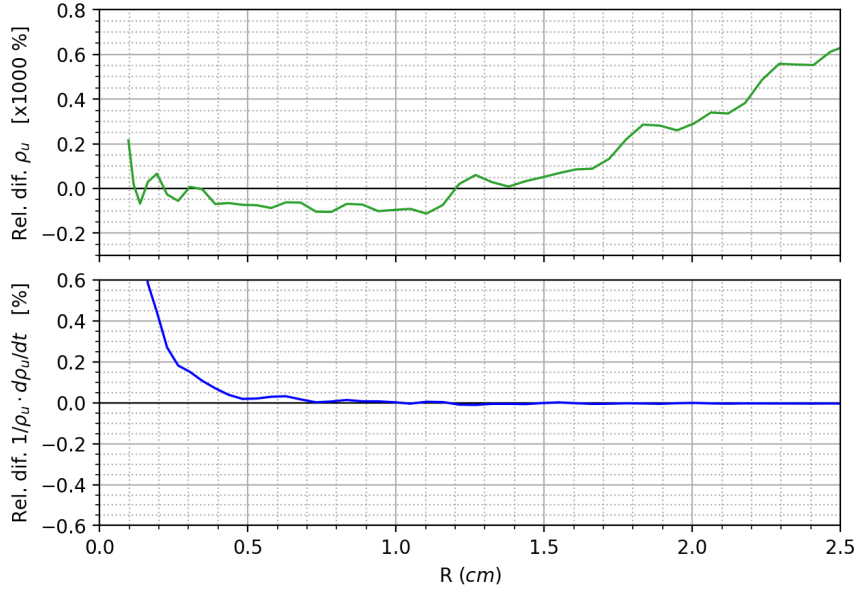


Figure (4) (Top) Relative difference of the numerical fresh gas density ρ_u calculated by Eq. 15 using DNS data and directly extracted from DNS database ($\phi = 1$). (Bottom) Influence of the position d on the evaluation of the compression term $1/\rho_u \cdot d\rho_u/dt$ of fresh gases. The relative difference of the value of this compression term computed with distance from tomographic radius $d = 3.5 \text{ mm}$ and $d = 1.2 \text{ mm}$ is reported as a function of the flame radius.

perfect agreement is reported as both the experimental and numerical data do overlap. From the previous statements, both the repeatability of experimental data as well as the accuracy of the post-processing techniques to access the compression term of Eq. (15) are demonstrated. From the thermodynamic perspective, the rate of change of the fresh gas density is linked to the rate of change of the pressure assuming isentropic compression, see Eq. (8). Figure 5 reports also experimental data for the compression term. Data corresponding to the time derivative of the pressure trace – isentropic compression – are widely dispersed. Therefore no trend of the rate of change of the pressure trace can be distinguished neither computed. The data lead to a high level of inaccuracy. It is worth noting that the accuracy of the pressure signal is responsible for this. Since the increase of the pressure signal is as low as 3 percents for a typical flame (radius of 2 cm for a stoichiometric CH_4/air flame), no pressure transducers were found to deal with small signal detection, high frequency sampling, huge

1
2
3
4
5
6
7
8
9 scaling range – up to several bar – and still affordable setup. Therefore, it
10 clearly appears that the measure of the pressure signal for the evaluation of the
11 compression term and the evaluation of Eq. (9) is not relevant enough. From an
12
13
14
410 experimental point of view, there is no possibility to achieve a reliable evaluation
15 of the consumption speed assuming isentropic compression hypothesis when
16 considering the constant pressure method in spherical expanding flames.
17
18

19 *4.4. Experimental uncertainties on stretched flame speeds*

20
21 Experimental uncertainties on the different stretched flame speeds are
22
415 computed as follows. First, we need to consider the uncertainties relative
23 to the operating conditions, mainly the initial mixture temperature, pressure,
24 equivalence ratio and spark energy. In addition to the intrinsic accuracy of each
25 sensor, the initial conditions can be slightly different from one experiment to
26 another. For this study, we consider a maximal variation of ± 1.5 K, ± 0.001 bar
27 and $\pm 1\%$ for initial temperature, pressure and equivalence ratio, respectively.
28
29
30
420 Spark energy, shape and volume may change also slightly from one ignition
31 to another one. These four sources of uncertainties may impact the flame
32 dynamic, and their contribution to the different flame speeds will be estimated
33 by performing a statistical analysis with a number of flame recordings per
34 condition, $N \geq 10$. The second source of uncertainty comes from the image
35 processing steps for each flame recording. Both flame radius and fresh gas
36 velocity determination from tomographic recordings are associated to individual
37 uncertainties coming from the capability of the routines to extract the quantities
38 of interest from noisy signals. The uncertainty of flame radii is estimated for each
39
40
41
42
43
44
45
46
47
430 flame contour by considering the relative distance between the flame contour and
48 the circle fit based on the least-square method. The mean relative uncertainty
49 over all the images is on the order of 0.03%. The uncertainty on the maximum
50 fresh gas velocity u_u includes the contribution of the sub-pixel fit of correlation
51 peak, the uncertainty in the flame front position after dewarping, and the
52
53
54
435 contribution of the six degree polynomial fit of the fresh gas velocity profile. The
55 mean relative uncertainty of u_u over all the images is on the order of 0.5%. Once
56
57
58

1
2
3
4
5
6
7
8
9
10
11
12
13
14
15
16
17
18
19
20
21
22
23
24
25
26
27
28
29
30
31
32
33
34
35
36
37
38
39
40
41
42
43
44
45
46
47
48
49
50
51
52
53
54
55
56
57
58
59
60
61
62
63
64
65

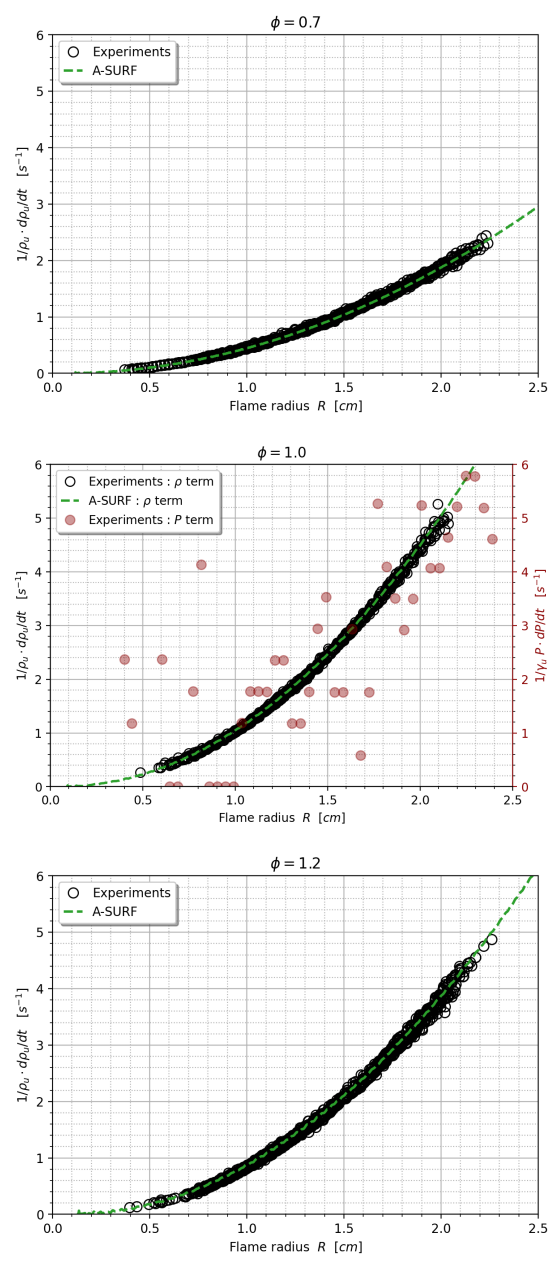


Figure (5) Comparison of the fresh gas density compression term from simulations and experimental data (based from more than 10 different flames) with respect to the experimental flame radius, for lean (Top), stoichiometric (Middle) and rich (Bottom) conditions. Comparison between the terms $1/\rho_u \cdot dp_u/dt$ and $1/\gamma_u P \cdot dP/dt$ for experiments when $\phi = 1.0$.

1
2
3
4
5
6
7
8
9 these uncertainties are evaluated, they are propagated when flame stretch and
10 the different flame speeds are computed, according to methodology suggested
11 by [31, 32]. Consequently, for each test, a one σ uncertainty is computed for
12
13
14
440 each instantaneous stretched flame speed S , hereafter $e(S)$, where S is either
15 $\widetilde{S}_{d,b}$, $\widetilde{S}_{d,u}$ or $\langle S_c \rangle$.
16

17 In the next section, the contribution of these two sources of uncertainties on
18 the different flame speeds is reported as follows. All the instantaneous stretched
19 flame speeds S_k are averaged per class of stretch of $8s^{-1}$ over the N tests,
20
21
22
445 weighted by their respective instantaneous uncertainty $e^2(S_k)$, according to [31,
23 32]:
24

$$\bar{S} = \frac{\sum_k \frac{S_k}{e^2(S_k)}}{\sum_k \frac{1}{e^2(S_k)}} \quad (16)$$

25
26
27
28
29
30 The corresponding variance is :
31

$$\sigma^2(\bar{S}) = \frac{1}{\sum_k \frac{1}{e^2(S_k)}} \quad (17)$$

32
33
34
35
36
37 Finally, an expanded uncertainty $U(\bar{S})$ of the averaged speed \bar{S} is calculated
38 from this variance $\sigma^2(\bar{S})$, and a coverage factor k , calculated from a Student's
39
40
41
42
43
44
450 law based on the number of value used on the average process ($k > 10$), and on
42 a level of confidence of 95%.
43

$$U(\bar{S}) = k\sigma(\bar{S}) \quad (18)$$

44
45
46
47
48
49
50
51
52
53
455 Consequently, \bar{S} will be plotted according to stretch with error bars equal to
49 $\pm U(\bar{S})$, that encompass large fraction (95%) of the distribution of values that
50 could reasonably be attributed to \bar{S} . Obviously, the higher the number of flame
51 recordings per condition, the lower the $\sigma(\bar{S})$.
52

53
54
55
56
57
58
59
60
61
62
63
64
65 In the following sections, stretch flame speeds, \bar{S} , will be fitted with linear or
non-linear models using the least squares method to find the extrapolated flame

1
2
3
4
5
6
7
8
9 speed and the corresponding Markstein length. The uncertainty on these two
10 parameters is estimated from the covariance matrix of the fit and the dispersion
11
12 of the residuals. All these data are reported in different tables below.
13
14

15 **5. Flame speed evaluations, and direct comparison with DNS**

16
17 In this section, the three different stretched flame speeds are experimentally
18 evaluated according to the previous developments for CH_4/air flames at
19 three different equivalence ratios. Extrapolated values are also compared
20
21 with numerical laminar burning velocity S_L^0 obtained from Cantera (freely
22
23 465 propagating 1D flame, with GRI3.0). Each comparison is followed by discussions
24 about the relevance of the methodology and the potential use of these flame
25 speeds for both laminar flame speed determination and use in some applications.
26
27 $\widetilde{S}_{d,b}$ is first presented to illustrate the capability of the DNS to reproduce
28
29 470 the flame dynamic in that geometrical configuration. From that preliminary
30 comparison, $\widetilde{S}_{d,u}$ is then discussed, followed by the new developments made to
31 estimate the spatially averaged consumption speed $\langle S_c \rangle$.
32
33
34
35

36 *5.1. Displacement speed relative to burned gases, $\widetilde{S}_{d,b}$*

37
38 Figure 6 presents a direct comparison of density weighted displacement speed
39
40 475 relative to burned gases for lean, rich and stoichiometric conditions. Flame
41 speeds are plotted versus flame stretch from ignition to the maximum flame
42 radius which can be experimentally observed. In order to avoid ignition and
43 confinement effects, a restricted range of flame stretch must be chosen for
44 extrapolation. There is a general agreement to select a minimum flame radius
45
46 of 10 mm and a maximum flame radius of 25% of the flame chamber radius
47
48 480 R_0 [10, 33–35]. This range is represented by filled circles in Figure 6. A
49 direct comparison between experimental stretched flame speed and DNS data
50 is performed and a very good agreement is then observed for all the equivalence
51 ratios. For rich and stoichiometric conditions, the difference is marginal,
52
53 especially for flame kernels free from ignition effects. For lean condition, the
54
55
56
57
58
59
60
61
62
63
64
65

1
2
3
4
5
6
7
8
9 difference is larger and on the order of 1 *cm/s*. Ignition of very lean mixtures
10 requires high amount of energy to get spherical kernels which may affect the
11 displacement speed $\widetilde{S}_{d,b}$ a little beyond the minimum flame radius of 1 *cm*.
12 For flame radii larger than 2 *cm*, the slope decreases progressively to become
13
14
15 strongly negative. This confinement effect is visible both from the experiments
490 and the simulations. This blind comparison confirms the capability of the 1D
16
17 spherical DNS with GRI3.0 kinetic scheme to reproduce the dynamic of the flame
18 front. Linear extrapolation (Eq. 19) at zero stretch for lean and stoichiometric
19 conditions, and a classical non-linear extrapolation (Eq. 20) for rich conditions
20
21
22
23 are used as recommended by [36].
495

$$\widetilde{S}_{d,b} = S_L^0 - \mathcal{L}_b K \quad (19)$$

$$\left(\frac{\widetilde{S}_{d,b}}{S_L^0}\right)^2 \ln\left(\frac{\widetilde{S}_{d,b}}{S_L^0}\right)^2 = -2\frac{\mathcal{L}_b K}{S_L^0} \quad (20)$$

24
25
26
27
28
29
30
31
32
33 It is worth noting that the Markstein Lengths \mathcal{L}_b in Eqs 19 and 20 are related
34 to the density weighted displacement speed relative to burned gases, and differ
35 from most of the data available in the literature by a factor equal to the density
36 ratio, since $\widetilde{S}_{d,b}$ is considered instead of $S_{d,b} = dR/dt$.
37
38

39
500 A deviation of S_L^0 from experiments with those from predicted by Cantera
40 simulation is observed for all the cases and it is about 2-3 *cm/s* (Table 1). This
41 difference in S_L^0 between experiments (based on outwardly propagating spherical
42 flame) and simulation (based on unstretched, adiabatic, freely-propagating
43 planar flame) is commonly observed in the literature ([34], Figure 3) and has
44
45
46
47
505 been explained by many possible experimental biases: mixture preparation,
48 ignition effect, radiation effect, extrapolation model, confinement effect. More
49
50 surprisingly, S_L^0 values extrapolated from DNS data with the same range of
51 flame stretch free from ignition and confinement effects are also lower than
52
53 Cantera values, whereas the same kinetic scheme is used. Similar behaviors were
54
55
56
57
58
59
60
61
62
63
64
65 observed previously for confined spherical expanding flames but never discussed.
510 For instance, stoichiometric methane/air flames were simulated by [11] with

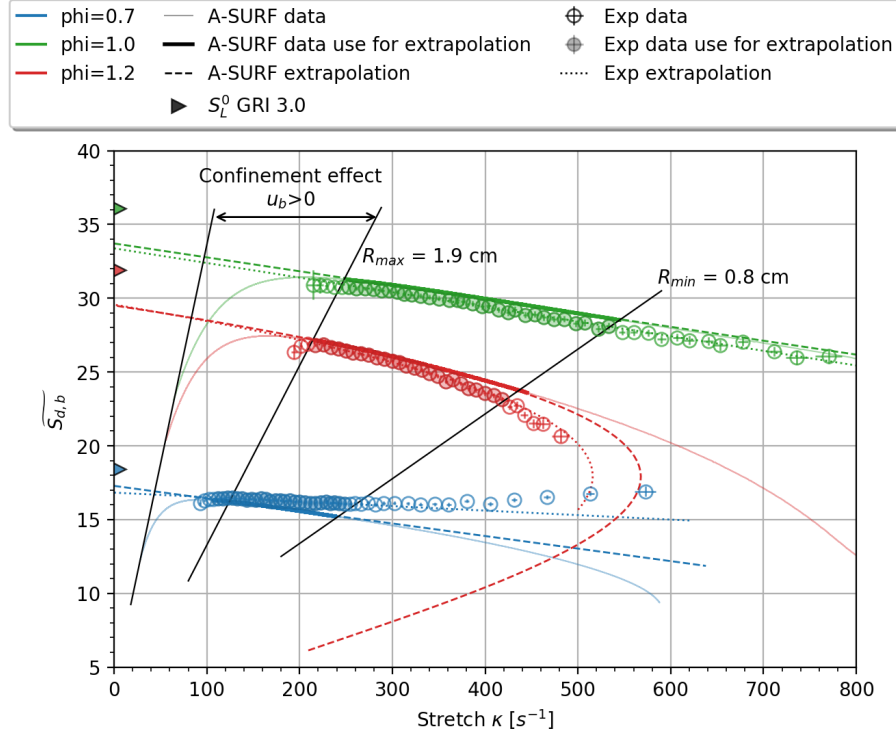


Figure (6) Evolution of $\widetilde{S}_{d,b}$ with flame stretch at different equivalence ratios.

GRI3.0 mechanism with larger radius combustion chamber. $S_{d,b}^0$ was estimated at 268 cm/s, leading to $S_L^0 = 35.45$ cm/s, which is below the target given by 1D planar flame calculation. Similar observations can be found in [37] and [39] still with GRI3.0.

		S_L^0 [cm/s]	$\sigma_{S_L^0}$ [cm/s]	\mathcal{L}_b [mm]	$\sigma_{\mathcal{L}_b}$ [mm]	fit
$\phi = 0.7$	Cantera	18.49	-	-	-	-
	Experiments	16.82	0.036	0.030	0.0024	Linear
	DNS	17.28	-	0.085	-	Linear
$\phi = 1.0$	Cantera	36.30	-	-	-	-
	Experiments	33.38	0.078	0.099	0.0022	Linear
	DNS	33.71	-	0.094	-	Linear
$\phi = 1.2$	Cantera	32.00	-	-	-	-
	Experiments	29.56	0.047	0.105	0.0011	Non-Linear
	DNS	29.50	-	0.095	-	Non-Linear

Table (1) Extrapolated flame speed from $\widetilde{S}_{d,b}$ and corresponding Markstein length, \mathcal{L}_b , obtained from Eq. 19 and 20 by fitting $\widetilde{S}_{d,b} = f(K)$ for tomographic radius between 0.8cm and 1.9cm.

1
2
3
4
5
6
7
8
9 *5.2. Displacement speed relative to fresh gases, $\widetilde{S}_{d,u}$*

10
11 Figure 7 reports the evolution of experimental and numerical $\widetilde{S}_{d,u}$ over flame
12 stretch rate at different equivalence ratios. As for $\widetilde{S}_{d,b}$, the flame speeds from
13 the 10 measurements are averaged per class of stretch of $8s^{-1}$. The statistical
14 approach used to report data allows a good and relevant comparison with the
15 DNS. As mentioned previously, the routines developed by Varea et al. [14] have
16 been improved to reduce shot to shot variation and reliability of post processing.
17 From Fig. 7, one can see an excellent agreement between both experimental and
18 DNS data. Different observations can be done from the evolution of $\widetilde{S}_{d,u}$ over
19 stretch. First, the sensitivity to the ignition stage seems to be lower than for
20 $\widetilde{S}_{d,b}$ since the flame speed spreads linearly towards smaller flame radii regardless
21 the equivalence ratio. Second, a lower sensitivity to flame confinement effect is
22 observed as the flame speed $\widetilde{S}_{d,u}$ behaves linearly for very large flame radii,
23 excepted when the thermodynamic conditions P and T differ drastically from
24 the initial ones. Hence, considering the flame radius range $R_{min} - R_{max} =$
25 $[0.8 - 2.4cm]$, extrapolations at zero stretch are more robust and less dependent
26 of the flame radii range. Similar behaviors are observed also for the DNS.
27 In order to be consistent to the extrapolation methodology used for $\widetilde{S}_{d,b}$, the
28 following linear extrapolation (Eq. 21) at zero stretch is used [2],
29
30
31
32
33
34
35
36
37
38
39
40

$$\widetilde{S}_{d,u} = S_L^0 - \mathcal{L}_u K \quad (21)$$

41
42
43
44
45
46
47
48
49
50
51
52
53
54
55
56
57
58
59
60
61
62
63
64
65

535 It is important to note that using traditional extrapolation formula for
536 $\widetilde{S}_{d,u}$ (affected by thermal dilation) is not strictly correct, as pointed out by
537 [38]. Consequently, such extrapolation performed (using a thermal dilatation
538 affected value) may result in errors as pointed out by [28]. However, the
539 zero stretch extrapolation of the experimental data converges with accuracy
540 to the Cantera 1D values. The target values are reached for both DNS and
541 experimental data for the three equivalence ratios. $\widetilde{S}_{d,u}$ measurement technique
542 is shown to be not affected by the small size of the combustion chamber and
543 therefore to confinement and ignition effects, allowing accurate measurements of

extrapolated values for low or intermediate chamber radii. Table 2 summarizes the corresponding Markstein Lengths following Eq. 21 from experimental and numerical data. One can see that both experimental and numerical values are in good agreement. Only few experimental data are available in the literature for comparison, but excellent agreement is found with previous works from the group, [14], as well as more recent works from Bradley et al. [15]. From these studies, \mathcal{L}_u for stoichiometric methane/air flame at ambient temperature and atmospheric pressure are very close to those obtained in this work, -0.12 mm and -0.11 mm , respectively. For their numerical work, Giannakopoulos et al. [2] demonstrated that flame sensitivities to stretch were more dependent to the isotherm chosen when the fresh gas side was used compared to the burned gas side. In this study, we show that experimental measurements can report quantitative and accurate data on $\widetilde{S}_{d,u}$ and its associated extrapolated value when care is taken on the experimental protocol and post processing. Moreover, as mentioned by Jayachandran et al. [28, 30] laminar burning velocities measured by $\widetilde{S}_{d,u}$ technique avoid any biases due to radiation, extrapolation procedure and density correction. Moreover, as long as inward flow exists due to confinement and/or sub or hyper adiabatic conditions [11], $\widetilde{S}_{d,u}$ technique seems to be a good candidate for accurate laminar burning velocities measurements. This is typically true when heavy/light fuels but also tailor made fuels are considered for which no kinetic schemes exist.

		S_L^0 [cm/s]	$\sigma_{S_L^0}$ [cm/s]	\mathcal{L}_u [mm]	$\sigma_{\mathcal{L}_u}$ [mm]
$\phi = 0.7$	Cantera	18.49	-	-	-
	Experiments	18.36	0.19	-0.194	0.014
	DNS	19.13	-	-0.135	-
$\phi = 1.0$	Cantera	36.30	-	-	-
	Experiments	35.72	0.48	-0.115	0.015
	DNS	36.71	-	-0.084	-
$\phi = 1.2$	Cantera	32.00	-	-	-
	Experiments	32.89	0.53	-0.069	0.019
	DNS	33.00	-	-0.047	-

Table (2) Extrapolated flame speed from $\widetilde{S}_{d,u}$ and corresponding Markstein length, \mathcal{L}_u , obtained from Eq. 21 by fitting $\widetilde{S}_{d,u} = f(K)$ for tomographic radius between 0.8 cm and 2.2 cm .

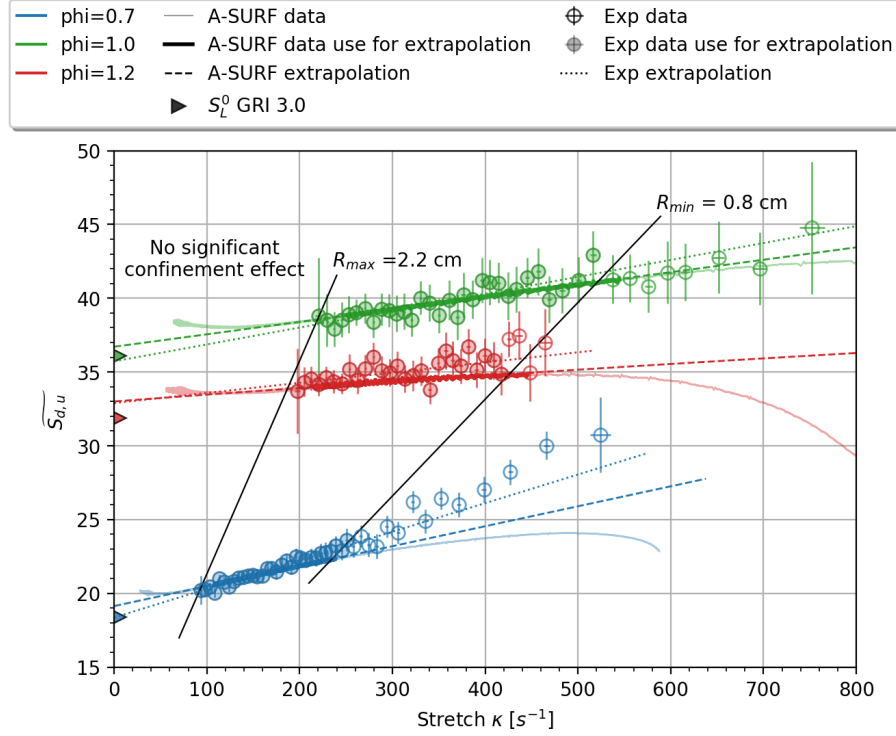


Figure (7) Direct comparison of density weighted displacement speed relative to fresh gases for experimental and DNS data.

5.3. Spatially averaged consumption speed, $\langle S_c \rangle$

The spatially averaged consumption speed of the deficient species is now reported from experimental measurements of flame radius R_T , obtained from tomographic recordings, and fresh gas density deduced from fresh gas velocity profile as presented above. This is reminded in Eq.22.

$$\langle S_c \rangle = \frac{dR_T}{dt} - \frac{(R_0^3 - R_T^3)}{3R_T^2} \frac{1}{\rho_u} \frac{d\rho_u}{dt} \quad (22)$$

We implicitly assume that the experimental flame radius R_T is equal to $R_{f,eq}$ in Eq. 7. This was already validated in [20]. Simultaneously, the spatially averaged consumption speed from the DNS can be exactly computed from the integral of the mass reaction rate of the deficient species, according to the

developments in [19] and [20]:

$$\langle S_{c,DNS} \rangle = -\frac{1}{\rho_u Y_{k,u} R_{f,k}^2} \int_0^{R_0} \dot{\omega}_k r^2 dr \quad (23)$$

575 Equality between Eq. 22 and Eq. 23 was already numerically demonstrated
in [20]. We present now the experimental measurements of $\langle S_c \rangle$ by Eq. 22
and the comparison with the DNS data from Eq.23. For the three different
equivalence ratios, the spatially averaged consumption speeds are reported
according to flame stretch (Figures 8, 9 and 10). At the same time, the first and
580 the second term of the RHS of Eq.22 are also plotted both from the experiments
and the DNS to validate the experimental determination of these two terms. $\langle S_c \rangle$
is calculated as the difference of two large numbers, and therefore its accuracy
will depend directly on the accuracy of each contribution. For the first term,
error bars are similar to those indicated for $\widetilde{S_{d,b}}$ which were mainly due to the
585 shot-to-shot repeatability, multiplied by the density ratio. The second term
has similar error bars. Both terms are well captured by the experiment, with
stretched values that are very close to the DNS (slightly underestimated for
 $\phi = 1.0$ and 1.2 , and quite clearly overestimated for $\phi = 0.7$). For high stretch
values, this difference slightly increases, before diverging when the influence
590 of ignition becomes predominant. The difference of these two contributions
gives the spatially averaged consumption speed $\langle S_c \rangle$, which is in very good
agreement with the consumption speed computed from the integral of the
reaction rate. For stretched flames free from confinement and ignition effects,
experiments and DNS values are superimposed. For $\phi = 0.7$, the agreement
595 is slightly worse, as already observed for $\widetilde{S_{d,b}}$. For this condition, ignition
effect seems to persist beyond the usual minimum value of flame radius. The
error bars on experimental $\langle S_c \rangle$ are slightly lower compared to those of the two
contributions, which underlines the compensating effect when considering the
shot to shot fluctuation. Stretched consumption speeds seem much less sensitive
600 to confinement effects than $\widetilde{S_{d,b}}$, with a globally linear behavior at large radii,
observed both numerically and experimentally, with the range of flame radius

accessible through the chamber. The extrapolated values are similar to each other, slightly lower than the values given by the 1D calculation by Cantera. The slopes are also well captured by the experiments.

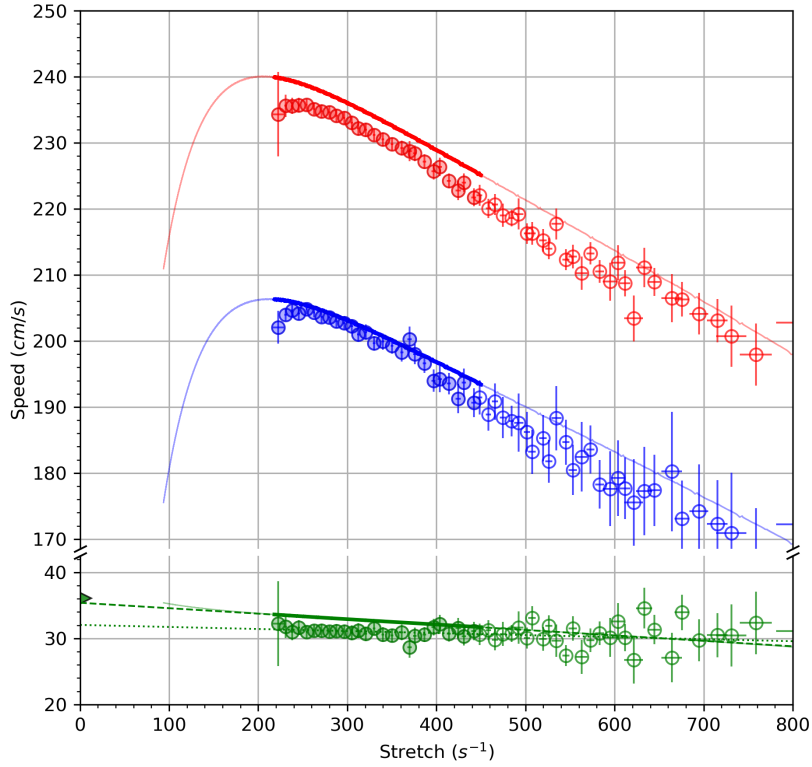


Figure (8) Direct comparison of spatially averaged consumption speed for experimental and DNS data, $\phi = 1.0$. DNS data are represented by continuous lines. Experimental data are reported in this figure with circle symbols. Red color is dR_T/dt , blue color is the density ratio term in Eq. 22 and the spatially averaged consumption speed is represented in green by using Eq. 22 for experiments and Eq. 23 for the DNS. Linear extrapolations over the bold line and filled symbols are reported in dotted and dashed lines.

605 Similarly to the density weighted displacement speeds, extrapolation at zero stretch of the spatially averaged consumption speed allows to introduce the Markstein length \mathcal{L}_c , according to the following linear equation,

$$\langle S_c \rangle = S_L^0 - \mathcal{L}_c K \quad (24)$$

Values of extrapolated flame speed and Markstein length are reported in

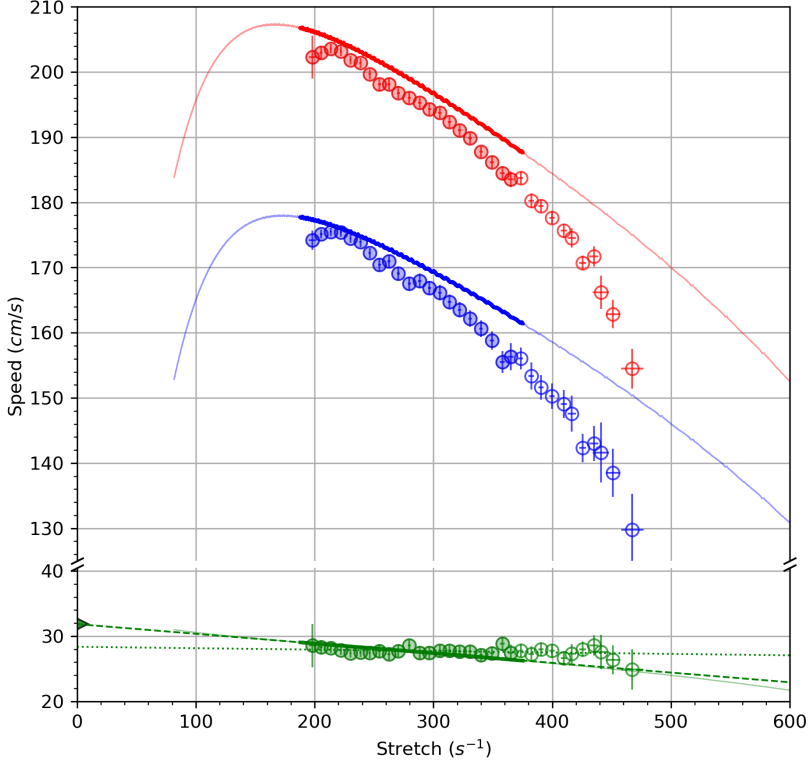


Figure (9) Direct comparison of spatially averaged consumption speed for experimental and DNS data, $\phi = 1.2$. DNS data are represented by continuous lines. Experimental data are reported in this figure with circle symbols. Red color is dR_T/dt , blue color is the density ratio term in Eq. 22 and the spatially averaged consumption speed is represented in green by using Eq. 22 for experiments and Eq. 23 for the DNS. Linear extrapolations over the bold line and filled symbols are reported in dotted and dashed lines.

Table 3.

		S_L^0 [cm/s]	$\sigma_{S_L^0}$ [cm/s]	\mathcal{L}_c [mm]	$\sigma_{\mathcal{L}_c}$ [mm]	R_T range [cm]
$\phi = 0.7$	Cantera	18.49	-	-	-	-
	Experiments	15.81	1.21	0.015	0.100	[1.4; 2.2]
	DNS	17.90	-	0.135	-	[1.4; 2.2]
$\phi = 1.0$	Cantera	36.30	-	-	-	-
	Experiments	31.88	0.54	0.028	0.017	[1.0; 2.2]
	DNS	35.40	-	0.084	-	[1.0; 2.2]
$\phi = 1.2$	Cantera	32.00	-	-	-	-
	Experiments	27.95	0.50	0.010	0.018	[1.0; 2.2]
	DNS	31.82	-	0.047	-	[1.0; 2.2]

Table (3) Extrapolated flame speed from $\langle S_c \rangle$ and corresponding Markstein length, \mathcal{L}_c , obtained from Eq. 24 by fitting $\langle S_c \rangle = f(K)$ on a specific tomographic radius range.

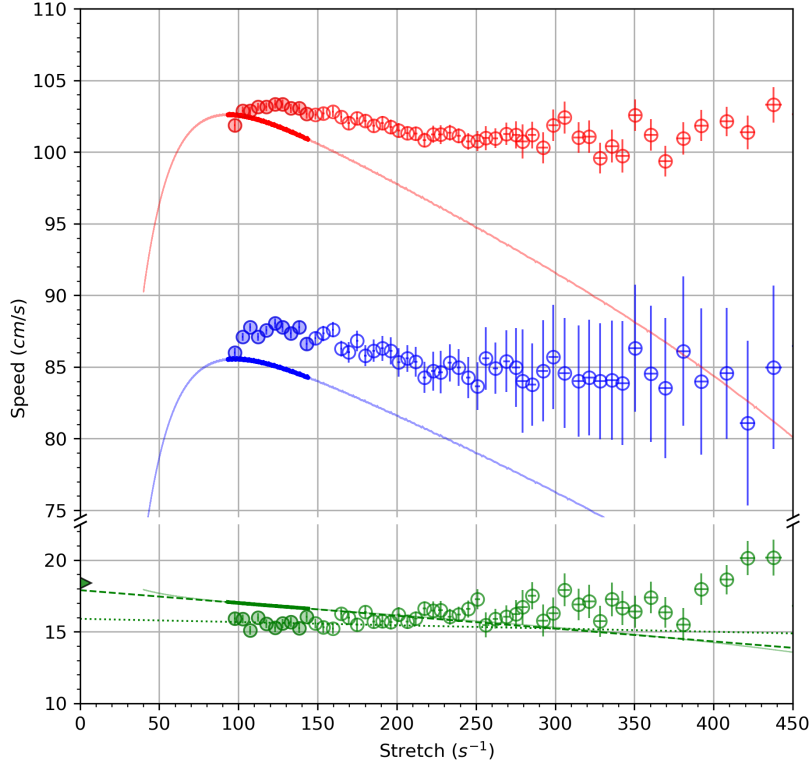


Figure (10) Direct comparison of spatially averaged consumption speed for experimental and DNS data, $\phi = 0.7$. DNS data are represented by continuous lines. Experimental data are reported in this figure with circle symbols. Red color is dR_T/dt , blue color is the density ratio term in Eq. 22 and the spatially averaged consumption speed is represented in green by using Eq. 22 for experiments and Eq. 23 for the DNS. Linear extrapolations over the bold line and filled symbols are reported in dotted and dashed lines.

610 The discussion about these results and the comparison with $\widetilde{S}_{d,b}$ requires
 611 some reminders about the definition of the spatially averaged consumption
 612 speed. As said previously, the spatially averaged flame speed is defined
 613 from the global consumption rate, obtained by integrating the fuel reaction
 614 rate throughout the whole flame volume, normalized by a reference surface
 615 $\mathcal{A} = 4\pi R^2$. As the spherical flame has a finite flame thickness which changes
 during its propagation, the identification of this reference surface (*i.e.* the
 isotherm) is delicate and can strongly impact the dependence of this spatially

averaged consumption speed on flame stretch,

$$\langle S_c \rangle_{R=R^*} = S_L^0 - \mathcal{L}_c^* K \quad (25)$$

In this equation $\langle S_c \rangle_{R=R^*}$ is the spatially averaged consumption speed with a reference surface equal to R^* and \mathcal{L}_c^* is the corresponding Markstein length. The influence of the isotherm on \mathcal{L}_c^* has been numerically shown by Giannakopoulos et al. [16] for propane / air mixtures, and a similar behavior is now presented for methane/air flames (Figure 11).

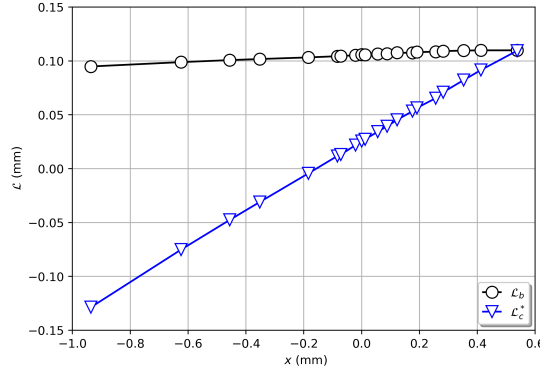


Figure (11) Effect of reference surface, expressed in flame radius and corresponding isotherm, on the Markstein lengths \mathcal{L}_c^* and \mathcal{L}_b . $\phi = 1$

In this work, it was decided to introduce a flame surface which does not suffer from any ambiguity and which is defined by an equivalent radius based on the total mass of fuel (if lean flame) or of oxidant (rich flame) [19, 20], $R^* = R_{f,k}$. For this particular value of R^* , Eq. 25 becomes equal to Eq. 24. We remind that this equivalent radius corresponds to an isotherm close to 600 K, and it is obtained experimentally from tomographic recordings. By considering Tables 1 and 3, one can see the very small differences between the Markstein lengths \mathcal{L}_b and \mathcal{L}_c .

The evolution of numerical data of \mathcal{L}_c^* and \mathcal{L}_b according to the isotherm of the flame radius is plotted in Figure 11. $x = 0$ refers to the location of the maximum heat release, and $x = 0.55$ corresponds to the fresh gas side. The difference between these two Markstein lengths decreases when one approaches

1
 2
 3
 4
 5
 6
 7
 8
 9 towards the gases fresh, and cancels out when R^* is close to $R_{f,k}$. Thus, with
 10 this reference surface, the spatially averaged consumption speed is expected to
 11 be very similar to $\widetilde{S}_{d,b}$. Note that even if the lengths \mathcal{L}_b and \mathcal{L}_c are similar, the
 12 spatial averaged consumption speed is not sensitive to confinement effects, and
 13
 14
 15
 16 640 seems to exhibit a linear behavior at high equivalence ratio, unlike $\widetilde{S}_{d,b}$. Note
 17 that this Markstein length \mathcal{L}_c is different from that introduced by asymptotic
 18 studies [16], where the *local* consumption speed is considered (Eq. 1). This
 19 Markstein length noted $\mathcal{L}_{c,Local}$ is systematically greater than the length \mathcal{L}_b
 20 and very weakly dependent on the fuel, according to the following relation [16],
 21
 22
 23

$$\mathcal{L}_b - \mathcal{L}_{c,Local} = \left(\frac{1}{\sigma - 1} \int_1^\sigma \frac{\tilde{\lambda}(x)}{x} dx \right) \cdot l_f \quad (26)$$

24
 25
 26
 27 645 where σ is the thermal expansion ratio, $\tilde{\lambda}$ is the non-dimensional thermal
 28 conductivity and l_f is the flame reaction zone thickness estimated from the ratio
 29 of the thermal diffusivity of the fresh gases with the laminar flame speed.
 30
 31
 32

6. Conclusion

33
 34
 35
 36 This paper highlights the experimental tools which have been developed for
 37
 38 650 measuring laminar flame speeds in the expanding flame velocity configuration
 39 (kinematic and kinetic velocities) whose definitions and expressions have been
 40 rigorously derived previously. These laminar flame speeds were measured for
 41 methane/air mixtures at different equivalence ratios and compared directly
 42 with DNS performed by A-SURF code simulating the exact geometry of the
 43
 44
 45
 46 655 combustion chamber, in spherical 1D coordinates. This numerical approach
 47 allowed validation of all the post-processing steps, giving access to the local
 48 fresh gas velocity at the entrance of the flame front, as well as to the density
 49 of the fresh gases, and the values of the stretched laminar flame speeds. With
 50 this numerical database, the experimental measurements enable the following
 51
 52
 53
 54 660 conclusions to be drawn about the relevance and the accuracy of the different
 55 flame speeds.
 56
 57
 58
 59
 60
 61
 62
 63
 64
 65

1
 2
 3
 4
 5
 6
 7
 8
 9 This work reports a new experimental approach to evaluate the spatially
 10 averaged consumption speed $\langle S_c \rangle$ for spherically expanding flames from
 11 tomographic flame radius and fresh gases density measurements, Eq. (22). This
 12 methodology was derived recently from the global reaction rate normalized
 13
 14 665 by a reference flame surface defined by an equivalent flame radius based on
 15 the total mass of fuel (if lean flame) or of oxidant (rich flame) [20]. The
 16 novelty of this work is associated to the experimental measurement of fresh
 17 gas density from the integration of the continuity equation through a material
 18 control volume. Considering the initial fresh gas density, the location of the
 19 boundary of the control volume and the fresh gas velocity, it is possible to
 20 report the temporal evolution of the fresh gas density with an excellent level
 21 of accuracy, as demonstrated by the direct comparison with the DNS. The
 22 spatially averaged consumption speed is very close to the flame speed $\widetilde{S}_{d,b}$
 23 with similar positive Markstein lengths. $\langle S_c \rangle$ is however less sensitive to flame
 24 confinement and behaves more linearly with flame stretch for rich conditions.
 25 Even interesting to report an experimental measurement of total fuel reaction
 26 rate, it seems therefore difficult to extend this technique to other fuel/air
 27 mixtures without any other preliminary validations, such as the equivalence
 28 between tomographic flame radius and the equivalent flame radius, $R_{f,k}$. It is
 29 also important to note that this spatially averaged consumption speed differs
 30 from the local consumption speed introduced in asymptotic theories and used
 31 in 1D configurations, and must be considered as complementary.
 32
 33
 34
 35
 36
 37
 38
 39
 40
 41
 42
 43
 44
 45
 46
 47
 48
 49
 50
 51
 52
 53
 54
 55
 56
 57
 58
 59
 60
 61
 62
 63
 64
 65

The displacement speed $\widetilde{S}_{d,u}$ requires an accurate measurement of the
 665 maximum velocity of the fresh gases at the entrance to the flame front. In
 this paper, an important improvement of post-processing tools was carried
 out and validated by a direct comparison with DNS simulations. To our
 knowledge, this is the first time that the fresh gas velocity profiles across the
 flame front in spherical expanding flames have been compared directly with
 690 DNS. The experimental fresh gas velocity profiles overlap perfectly with the
 DNS, and the agreement with the stretched flame speed $\widetilde{S}_{d,u}$ is excellent. For
 the operating conditions (quasi equi-diffusive fuel/air mixtures), this flame speed

1
2
3
4
5
6
7
8
9 behaves linearly with stretch, and allows a direct estimation of the laminar
10 burning velocity S_L^0 by a linear extrapolation. This quantity is not influenced
11
12
13
14
15
16
17
18
19
20
21
22
23
24
25
26
27
28
29
30
31
32
33
34
35
36
37
38
39
40
41
42
43
44
45
46
47
48
49
50
51
52
53
54
55
56
57
58
59
60
61
62
63
64
65

695 by confinement effects and does not underestimate the extrapolated flame speed
 S_L^0 . Extension of this linear extrapolation to non equi-diffusive fuel/air mixtures
requires additional tests and discussion. It is also worth noting that this method
presents a quite important scatter in spite of the improvements made. It is then
necessary to carry out a larger number of tests (here about ten) to converge.

700 The flame speed $\widetilde{S}_{d,b}$ is very easy to measure with the assumptions usually
made (burnt gases at equilibrium and at rest), but remains very sensitive to
the effects of flame confinement. In this geometry, extrapolation at zero stretch
leads to a systematic underestimation of the laminar burning velocity S_L^0 of the
order of 1 to 3 *cm/s*, regardless of the equivalence ratio of the mixture. For small
705 combustion chambers, this effect is noticeable even when respecting the classic
radius range criteria for extrapolation. A careful look of the literature also shows
that this phenomenon is observed even for larger combustion chambers. This
quantity also requires an accurate knowledge of the fuel composition in order to
determine the density of the burnt gases by a chemical equilibrium calculation.
710 These remarks partly explain the disparities observed in the values reported in
recent years.

Acknowledgements

Financial supports from the French National Research Agency, under the
project 'RAF BIOALG (ANR-18-CE43-0009)' and National Natural Science
715 Foundation of China (no. 51861135309) are gratefully acknowledged.

References

- [1] T. Poinso, D. Veynante, Theoretical and Numerical Combustion, Third
Edition (www.cerfacs.fr/elearning), 2011.
- [2] G. K. Giannakopoulos, A. Gatzoulis, C. E. Frouzakis, M. Matalon, A. G.
720 Tomboulides, Consistent definitions of “flame displacement speed” and

1
2
3
4
5
6
7
8
9
10
11
12
13
14
15
16
17
18
19
20
21
22
23
24
25
26
27
28
29
30
31
32
33
34
35
36
37
38
39
40
41
42
43
44
45
46
47
48
49
50
51
52
53
54
55
56
57
58
59
60
61
62
63
64
65

“markstein length” for premixed flame propagation, *Combust. Flame* 162 (2015) 1249–1264.

[3] F. N. Egolfopoulos, N. Hansen, Y. Ju, K. Kohse-Höinghaus, C. K. Law, F. Qi, Advances and challenges in laminar flame experiments and implications for combustion chemistry, *Prog. Energy Combust. Sci.* 43 (2014) 36–67.

[4] N. Hinton, R. Stone, Laminar burning velocity measurements of methane and carbon dioxide mixtures (biogas) over wide ranging temperatures and pressures, *Fuel* 116 (2014) 743–750.

[5] C. Xiouris, T. Ye, J. Jayachandran, F. Egolfopoulos, Laminar flame speeds under engine-relevant conditions: Uncertainty quantification and minimization in spherically expanding flame experiments, *Combust. Flame* 163 (2016) 270 – 283.

[6] F. Halter, Z. Chen, G. Dayma, C. Bariki, Y. Wang, P. Dagaut, C. Chauveau, Development of an optically accessible apparatus to characterize the evolution of spherically expanding flames under constant volume conditions, *Combust. Flame* 212 (2020) 165–176.

[7] A. P. Kelley, J. K. Bechtold, C. K. Law, Premixed flame propagation in a confining vessel with weak pressure rise, *J. Fluid Mech.* 691 (2012) 26–51.

[8] W. Liang, F. Wu, C. K. Law, Extrapolation of laminar flame speeds from stretched flames: Role of finite flame thickness, *Proc. Combust. Inst.* 36 (2017) 1137–1143.

[9] T. Shu, Y. Xue, W. Liang, Z. Ren, Extrapolations of laminar flame speeds from expanding spherical flames based on the finite-structure stretched flames, *Combust. Flame* 226 (2021) 445–454.

[10] M. P. Burke, Z. Chen, Y. Ju, F. L. Dryer, Effect of cylindrical confinement on the determination of laminar flame speeds using outwardly propagating flames, *Combust. Flame* 156 (2009) 771–779.

- 1
2
3
4
5
6
7
8
9 [11] M. Faghih, Z. Chen, J. Huo, Z. Ren, C. K. Law, On the determination
10 of laminar flame speed from low-pressure and super-adiabatic propagating
11 750 spherical flames, *Proc. Combust. Inst.* 37 (2019) 1505–1512.
- 12
13
14 [12] Z. Chen, Effects of radiation and compression on propagating spherical
15 flames of methane/air mixtures near the lean flammability limit, *Combust.*
16 *Flame* 157 (2010) 2267–2276.
- 17
18
19 [13] S. Balusamy, A. Cessou, B. Lecordier, Direct measurement of local
20 755 instantaneous laminar burning velocity by a new piv algorithm, *Exp. Fluids*
21 50 (2011) 1109–1121.
- 22
23
24 [14] E. Varea, V. Modica, A. Vandel, B. Renou, Measurement of laminar
25 burning velocity and markstein length relative to fresh gases using a
26 new postprocessing procedure: Application to laminar spherical flames for
27 760 methane, ethanol and isooctane/air mixtures, *Combust. Flame* 159 (2012)
28 577–590.
- 29
30
31 [15] D. Bradley, M. Lawes, M. E. Morsy, Flame speed and particle image
32 velocimetry measurements of laminar burning velocities and markstein
33 numbers of some hydrocarbons, *Fuel* 243 (2019) 423–432.
- 34 765
35
36 [16] G. K. Giannakopoulos, C. E. Frouzakis, S. Mohan, A. G. Tomboulides,
37 M. Matalon, Consumption and displacement speeds of stretched premixed
38 flames - theory and simulations, *Combust. Flame* 208 (2019) 164–181.
- 39
40
41 [17] E. F. Fiock, C. F. Marvin, The measurements of flame speed, *Chem. Rev.*
42 21 (1937) 367–387.
- 43 770
44
45 [18] D. Bradley, A. Mitcheson, Mathematical solutions for explosions in
46 spherical vessels, *Combust. Flame* 26 (1976) 201–217.
- 47
48
49 [19] A. Bonhomme, L. Selle, T. Poinso, Curvature and confinement effects
50 for flame speed measurements in laminar spherical and cylindrical flames,
51 *Combust. Flame* 160 (2013) 1208–1214.
- 52
53
54
55
56 775
57
58
59
60
61
62
63
64
65

- 1
2
3
4
5
6
7
8
9 [20] A. Lefebvre, H. Larabi, V. Moureau, G. Lartigue, E. Varea, V. Modica,
10 B. Renou, Formalism for spatially averaged consumption speed considering
11 spherically expanding flame configuration, *Combust. Flame* 173 (2016)
12 235–244.
13
14
15
16 780 [21] G. E. Andrews, D. Bradley, Determination of burning velocities: A critical
17 review, *Combust. Flame* 18 (1972) 133–153.
18
19 [22] E. Varea, V. Modica, B. Renou, A. M. Boukhalfa, Pressure effects on
20 laminar burning velocities and markstein lengths for isooctane–ethanol–air
21 mixtures, *Proc. Combust. Inst.* 34 (2013) 735–744.
22
23
24
25 785 [23] Z. Chen, M. P. Burke, Y. Ju, Effects of lewis number and ignition energy
26 on the determination of laminar flame speed using propagating spherical
27 flames, *Proc. Combust. Inst.* 32 (2009) 1253–1260.
28
29
30 [24] G. Smith, D. Golden, M. Frenklach, N. Moriarty, B. Eiteneer,
31 M. Goldenberg, C. Bowman, R. Hanson, S. Song, W. G. Jr., V. Lissianski,
32 Z. Qin, Gri-mech homepage, http://www.me.berkeley.edu/gri_mech/ (Gas
33 790 Research Institute).
34
35
36
37 [25] Y. Wang, A. Movaghar, Z. Wang, Z. Liu, W. Sun, F. N. Egolfopoulos,
38 Z. Chen, Laminar flame speeds of methane/air mixtures at engine
39 conditions: Performance of different kinetic models and power-law
40 correlations, *Combustion and Flame* 218 (2020) 101–108.
41 795
42
43
44 [26] H. Yu, W. Han, J. Santner, X. Gou, C. H. Sohn, Y. Ju, Z. Chen,
45 Radiation-induced uncertainty in laminar flame speed measured from
46 propagating spherical flames, *Combustion and Flame* 161 (2014)
47 2815–2824.
48
49
50
51 800 [27] D. G. Goodwin, R. L. Speth, H. K. Moffat, B. W. Weber, Cantera: An
52 object-oriented software toolkit for chemical kinetics, thermodynamics,
53 and transport processes, <https://www.cantera.org>, 2021. doi:10.5281/
54 zenodo.4527812, version 2.5.1.
55
56
57
58
59
60
61
62
63
64
65

- 1
2
3
4
5
6
7
8
9 [28] J. Jayachandran, R. Zhao, F. N. Egolfopoulos, Determination of laminar
10 flame speeds using stagnation and spherically expanding flames: Molecular
11 805 transport and radiation effects, *Combust. Flame* 161 (2014) 2305–2316.
12
13
14 [29] E. Varea, J. Beeckmann, H. Pitsch, Z. Chen, B. Renou, Determination
15 of burning velocities from spherically expanding h₂/air flames, *Proc.*
16 *Combust. Inst.* 35 (2015) 711–719.
17
18
19 [30] J. Jayachandran, A. Lefebvre, R. Zhao, F. Halter, E. Varea, B. Renou,
20 810 F. N. Egolfopoulos, A study of propagation of spherically expanding
21 and counterflow laminar flames using direct measurements and numerical
22 simulations, *Proc. Combust. Inst.* 35 (2015) 695–702.
23
24
25
26 [31] GUM: Guide to the expression of uncertainty in measurement, Joint
27 Committee for Guides in Metrology, 2008.
28 815
29
30 [32] I. Hughes, T. Hase, *Measurements and their Uncertainties. A practical*
31 *guide to modern error analysis*, Oxford University Press, 2010.
32
33
34 [33] D. Bradley, P. H. Gaskell, X. J. Gu, Burning velocities, markstein lengths,
35 and flame quenching for spherical methane-air flames: A computational
36 study, *Combust. Flame* 104 (1996) 176–198.
37 820
38
39 [34] Z. Chen, On the accuracy of laminar flame speeds measured from outwardly
40 propagating spherical flames: Methane/air at normal temperature and
41 pressure, *Combust. Flame* 162 (2015) 2442–2453.
42
43
44 [35] T. Sikes, M. S. Mannan, E. L. Petersen, An experimental study: laminar
45 flame speed sensitivity from spherical flames in stoichiometric ch₄-air
46 825 mixtures, *Combust. Sci. Technol.* 190 (2018) 1594–1613.
47
48
49
50 [36] A. P. Kelley, C. K. Law, Nonlinear effects in the extraction of laminar
51 flame speeds from expanding spherical flames, *Combust. Flame* 156 (2009)
52 1844–1851.
53
54
55
56
57
58
59
60
61
62
63
64
65

1
2
3
4
5
6
7
8
9
10
11
12
13
14
15
16
17
18
19
20
21
22
23
24
25
26
27
28
29
30
31
32
33
34
35
36
37
38
39
40
41
42
43
44
45
46
47
48
49
50
51
52
53
54
55
56
57
58
59
60
61
62
63
64
65

830 [37] Z. Chen, On the extraction of laminar flame speed and markstein length
from outwardly propagating spherical flames, *Combust. Flame* 158 (2011)
291–300.

[38] J. H. Tien, M. Matalon, On the burning velocity of stretched flames,
Combust. Flame 84 (1991) 238–248.

835 [39] J. Beeckmann, R. Hesse, J. Schaback, H. Pitsch, E. Varea, N. Chaumeix,
Flame propagation speed and markstein length of spherically expanding
flames: Assessment of extrapolation and measurement techniques, *Proc.*
Combust. Inst. 37 (2019) 1521–1528.

Declaration of interests

The authors declare that they have no known competing financial interests or personal relationships that could have appeared to influence the work reported in this paper.

The authors declare the following financial interests/personal relationships which may be considered as potential competing interests: